

Supplementary Materials for
**Structural analysis of HER2-trastuzumab complex reveals receptor
conformational adaptation**

Santiago Vacca *et al.*

Corresponding author: Jose M. Carazo, carazo@cnb.csic.es; Ohad Medalia, omedalia@bioc.uzh.ch;
Andreas Plückthun, plueckthun@bioc.uzh.ch

Sci. Adv. **11**, eadu9945 (2025)
DOI: 10.1126/sciadv.adu9945

The PDF file includes:

Supplementary Methods
Figs. S1 to S9
Legend for movie S1
References

Other Supplementary Material for this manuscript includes the following:

Movie S1

Supplementary Methods

Expression of MSP1D1ΔH5

The pellet of *E. coli* BL21Gold(DE3) that was harvested after expression of MSP1D1ΔH5 containing a TEV-cleavable his-tag, described by Schuster et al. (81), was kindly provided by Dr. Matthias Schuster, Department of Chemistry, University of Zurich, Switzerland. The construct was expressed for 4 h in BL21(DE3) cells in TB media at 37°C with induction at OD₆₀₀ = 2 in a 5 L Biostat A bioreactor (81).

Purification of MSP1D1ΔH5

The purification was performed at 4°C with precooled buffers, similar to the protocol described in (81). The cell pellet with expressed MSP1D1ΔH5 was resuspended with 4 ml/g of pellet in MSP lysis buffer (50 mM Tris-Cl (pH 8), 300 mM NaCl, 15 mM imidazole, 2% (v/v) Triton X-100 (Anatrace)). The resuspension was supplemented with 1 mM PMSF (Carl Roth), 2 mg/ml lysozyme (Sigma-Aldrich), 10 mM MgCl₂, and 50 μg/ml of DNase I (Roche). The cells were subsequently lysed by sonication (Branson sonifier, 40% output, 1 s on, 3 s off) on ice, and insoluble material was removed by centrifugation at 18,000 rpm in an SS-34 rotor for 30 minutes at 4°C. The supernatant was loaded onto 3 × 5 ml HisTrap HP columns (Cytiva) that were pre-equilibrated with MSP Triton buffer (20 mM Tris-Cl (pH 8), 300 mM NaCl, 1% (v/v) Triton X-100). After column binding, the columns were washed with 10 CVs of MSP Triton buffer, followed by 10 CVs of MSP cholate buffer (20 mM Tris-Cl (pH 8), 300 mM NaCl, 50 mM Na-cholate (Carl Roth)), 10 CVs of MSP buffer (20 mM Tris-Cl (pH 8), 300 mM NaCl), and 10 CVs of MSP wash buffer (20 mM Tris-Cl (pH 8), 300 mM NaCl, 50 mM imidazole). The MSP1D1ΔH5 was then eluted with MSP elution buffer (20 mM Tris-Cl (pH 8), 300 mM NaCl, 400 mM imidazole).

The elution was supplemented with 1 mM EDTA and dialyzed at 4°C for 2 h in 2 L MSP dialysis buffer (10 mM Tris (pH 8), 150 mM NaCl) using a 6-8 kDa dialysis membrane (Spectra/Por). After determining the protein concentration, TEV protease (kindly provided by Dr. Matthias Schuster) was added to the protein in the dialysis membrane in a 1:50 (w/w) ratio, and subsequently dialyzed overnight at room temperature in MSP dialysis buffer supplemented with 0.5 mM DTT. After the dialysis, the sample was subsequently loaded onto 3 × 5 ml HisTrap HP columns pre-equilibrated with MSP dialysis buffer. The flow-through was collected and dialyzed overnight in nanodisc buffer (20 mM Tris-Cl (pH 8), 50 mM NaCl) at room temperature. The protein was concentrated to 2-5 mg/ml with a 10 kDa MWCO Amicon concentrator (Merck Millipore). After concentration, the protein was aliquoted and frozen with liquid nitrogen for storage at -80°C.

Reconstitution of HER2 in MSP nanodiscs

Chloroform-solubilized L- α -phosphatidylcholine (EggPC; Avanti Polar Lipids 840051C) was placed in a glass tube under a nitrogen stream to dry up the chloroform, forming a thin lipid film. Residual solvent was removed by placing the tube under a vacuum overnight. After drying the lipid films, the EggPC was solubilized with sodium cholate buffer (20 mM Tris-Cl (pH 7.4), 200 mM Na-cholate) to give a 50 mM EggPC stock solution.

Purified HER2, purified MSP1D1ΔH5, and solubilized EggPC were then mixed to a final HER2:MSP:lipid molar ratio of 1:10:400 with a final Na-cholate concentration of 17 mM

and final mixture volume of 100 μ l, for a 1 hour incubation at 4°C. Up to 10 \times 100 μ l reconstitution mixtures were prepared in Eppendorf tubes. Biobeads (50% v/v) were then added to each of the Eppendorf tubes and incubated for 16 hours at 4°C while mixing. The Biobeads were then removed, and the protein samples were combined and centrifuged at 22,000 \times g for 5 minutes at 4°C. The supernatant was subsequently collected, loaded in 50 μ l aliquots onto a Superose 6 Increase 5/150 GL column (Cytiva) pre-equilibrated with Superose buffer (40 mM Tris-Cl (pH 7.5), 300 mM NaCl). Fractions corresponding to the nanodisc-reconstituted receptor from each individual gel filtration run were combined and concentrated to 0.3 mg/ml for subsequent cryo-EM analysis.

Expression of Saposin A

A pNIC28-Bsa4 plasmid encoding the Prosaposin gene region (residues 60 to 140) coding for saposin A with an N-terminal TEV-cleavable His₆-tag, detailed by Flayhan et al. (82), was a gift from Dr. Christian Löw, EMBL, Hamburg, Germany. *E. coli* Rosetta-gami 2(DE3) cells were transformed with the plasmid DNA, and an overnight preculture was prepared using LB medium supplemented with 30 μ g/ml kanamycin, 25 μ g/ml chloramphenicol, and 12.5 μ g/ml tetracycline. After an overnight incubation at 37°C under constant shaking, the culture was diluted with TB medium supplemented with the antibiotics, to an OD_{600nm} of 0.05. Cells were grown at 37°C while shaking and induced with 1 mM sterile-filtered isopropyl- β -D-thiogalactopyranoside (IPTG) at OD_{600nm} between 0.8 and 1. After a four-hour incubation at 37°C, the cells were harvested by centrifugation at 4000 \times g for 15 minutes at 4°C. The cells were then washed with PBS, and the pellet was subsequently flash-frozen in liquid nitrogen and stored at -80°C.

Purification of Saposin A

The purification was performed similarly to that described in (82). The frozen cell pellet was thawed and resuspended with 5 ml/g of pellet with saposin lysis buffer (20 mM sodium phosphate (Na-P; pH 7.5), 300 mM NaCl, 15 mM imidazole, 5% glycerol, 20 μ g/ml DNase I, 5 mM MgCl₂, 1 mg/ml lysozyme, 5 μ g/ml Leupeptin (Sigma-Aldrich), 1 μ g/ml Pepstatin A, 24 μ g/ml Pefabloc SC). The cells were lysed by sonication for 9 minutes on ice with a Sonifier 250 (Branson) at a duty cycle of 50% and output 5, with a 5-minute cooldown for every 3 minutes of sonication. Cell debris and unlysed cells were removed by centrifugation at 4000 rpm (F14-14 \times 50cy rotor; ThermoFisher) for 30 minutes at 4°C. The supernatant was collected and incubated in a 75-80°C water bath for 10 minutes and subsequently centrifuged at 30,000 \times g for 20 minutes at 4°C. The supernatant was subsequently incubated for 1 hour while rolling at room temperature with Ni-NTA Superflow resin (Qiagen) (2 ml of resin for every 50 ml of lysate), pre-equilibrated with saposin wash buffer 1 (20 mM Na-P (pH 7.5), 300 mM NaCl, 15 mM imidazole, 5% glycerol). After incubation, the mixture was distributed into empty PD-10 columns (Cytiva, 17-0435-01) to discard the flow-through by gravity flow. The resin was washed with 15 CVs of saposin wash buffer 1, followed by 15 CVs of saposin wash buffer 2 (20 mM Na-P (pH 7.5), 300 mM NaCl, 30 mM imidazole, 5% glycerol). The protein was then eluted with 5 CVs of saposin elution buffer (20 mM Na-P (pH 7.5), 150 mM NaCl, 400 mM imidazole, 5% glycerol).

TEV protease was added to the eluate to remove the His₆-tag, which was then dialyzed overnight at room temperature against 1 L saposin dialysis buffer (20 mM Na-P (pH 7.5), 300 mM NaCl, 15 mM imidazole, 5% glycerol) using a 3.5 kDa MWCO dialysis membrane. The dialyzed protein was then applied to Ni-NTA resin pre-equilibrated with saposin dialysis buffer, and incubated with the resin while rolling for 1 hour at 4°C. The mixture was then transferred to an open gravity-flow column, and the flow-through containing the cleaved protein was collected. The resin was next washed with 5 ml of saposin wash buffer 1, and the wash flow-through was combined with the cleaved protein. The protein was then concentrated to 5 ml with a 3000 MWCO Amicon Ultra-15 concentrator, and subsequently loaded to a HiLoad 16/600 Superdex 75 pg column (Cytiva) pre-equilibrated with saposin gel filtration buffer (20 mM HEPES (pH 7.5), 150 mM NaCl). The purified protein was immediately used for reconstitution of HER2 into saposin A nanodiscs.

Reconstitution of HER2 in Saposin A nanodiscs

EggPC lipid was prepared as described above for HER2 reconstitution in MSP-based nanodiscs. Chloroform-solubilized EggPC was placed in a glass tube under a nitrogen stream to dry up the chloroform, forming a thin lipid film. Residual solvent was removed by placing the tube under a vacuum overnight. After drying the lipid films, the EggPC was solubilized with sodium cholate buffer to a 50 mM EggPC stock concentration.

Purified HER2, purified saposin A, and solubilized EggPC were then mixed to a final HER2:saposin:lipid molar ratio of 1:18:216 with a final mixture volume of 100 µl, and incubated for 1 hour at 4°C. Up to 10 × 100 µl reconstitution mixtures were prepared in Eppendorf tubes. Biobeads (50% v/v) were then added to each of the Eppendorf tubes and incubated for 16 hours at 4°C while mixing. The Biobeads were then removed, and the protein samples were combined and centrifuged at 22,000 × g for 5 minutes at 4°C. The supernatant was subsequently collected, loaded in 50 µl aliquots onto a Superose 6 Increase 5/150 GL pre-equilibrated with saposin Superose buffer (40 mM HEPES (pH 7.5), 300 mM NaCl). Fractions corresponding to the nanodisc-reconstituted receptor from each individual gel filtration run were combined and concentrated to 0.4 mg/ml for subsequent cryo-EM analysis.

Full-length 3D model preparation

This model is merely meant as an indication about the likelihood of steric clashes and should therefore not be interpreted beyond this. Since the connection between the transmembrane region and the ECD is flexible, we have to consider a range of possibilities, and therefore, the following approach was used. It should be noted that a modelling of the full receptors with AlphaFold 3 does not properly account for the orientational and conformational restrictions imposed by the membrane plane, necessitating this step-wise approach.

All residue numberings in this section correspond to the residue numbers in UniProt P04626-1 for HER2 and UniProt P21860-1 for HER3. For the preparation of the predicted model of the ligand-independent HER2-HER3 full-length heterodimer, HER2 residues 526-1029 and HER3 residues 569-979 were predicted with the AlphaFold Multimer (83, 84) software (v. 2.2.0). The C-terminal domain boundaries of HER2 and HER3 are the ends of the folded kinase domains, reflecting the different lengths of the kinase domain sequences for both receptors. The unstructured C-terminal tails were not included.

As the models will have uncertainty primarily in the flexible region that would link the transmembrane domains to the ECD, we took the following approach. Only a portion of subdomain IV of the extracellular domains, for both HER2 and HER3, were included in the prediction of the C-terminal part. This prediction of the HER2-HER3 heterodimer was made with an output of 25 predicted models. This run was repeated four times to observe consistency for a total of 100 predicted models of the same sequence. Of the 100 predicted models, 94 did not have reasonable orientations for what would be expected of an EGFR-family heterodimer, while 6 appeared reasonable when compared to the orientations observed for the HER1 homodimer in the negative stain 2D classifications determined by Mi et al. (42). These six models of the membrane and C-terminal part will be referred to as "AF1 models".

Our HER2 ECD structures of both the compact and extended conformations were superimposed with PyMOL on AF1 models via HER2 residues 526-624. The tethered HER3 crystal structure (PDB ID: 4LEO) was superimposed on residues 569-630 of the AF1 models. The Fab fragment bound to the HER3 in the PDB structure was removed. In all cases, there were clashes not only between the HER2-bound TZB and the HER3 ECD, but also between the HER2 ECD and the tethered HER3 ECD crystal structure. Additional AlphaFold structures of HER2 residues 526-684 were therefore generated, to obtain different predictions of the flexible linkage region. These models will be referred to as "AF2 models".

Each AF2 model was superimposed via the transmembrane domains on one AF1 model. The compact and extended conformations of the HER2 ECD were superimposed on the AF2 models via residues 526-624. AF2 models, for which superposition of the HER2 ECD would result in an ECD orientation that would potentially clash with the cell membrane, or clash with the tethered HER3 ECD, were discarded. The AF2 model which did not result in HER2 ECD clashes with the tethered HER3 ECD was retained (Fig. S7C & S8C).

The HER2 flexible region on the AF1 model was then flexibly adjusted in PyMOL to approximately fit the newly predicted AF2 flexible region. As a quality check of the remaining predicted regions of the AF1 model, the crystal structure of the HER3-HER1 kinase heterodimer (PDB ID: 4RIW (85)), the crystal structure of the HER2 kinase domain (PDB ID: 3PP0 (33)), the NMR structure of the HER3 transmembrane domain (PDB ID: 2L9U (86)), and the NMR structure of the HER2 transmembrane domain (PDB ID: 2KS1 (87)), were superimposed on the AF1 model, and the resulting RMSDs were noted to be 0.638, 0.581, 1.576, and 1.807 respectively. To simplify the model, all superimposed structures, including the AF2 model, were removed, and the HER2 compact and extended ECD structures were superimposed once more on the AF1 model, with its adjusted HER2 flexible linkage, and RMSD values of 1.212 and 2.141 respectively. The final schematic model of the ligand-independent HER2-HER3 heterodimer was visualized in UCSF ChimeraX (88) to produce Fig. S7E & S8E.

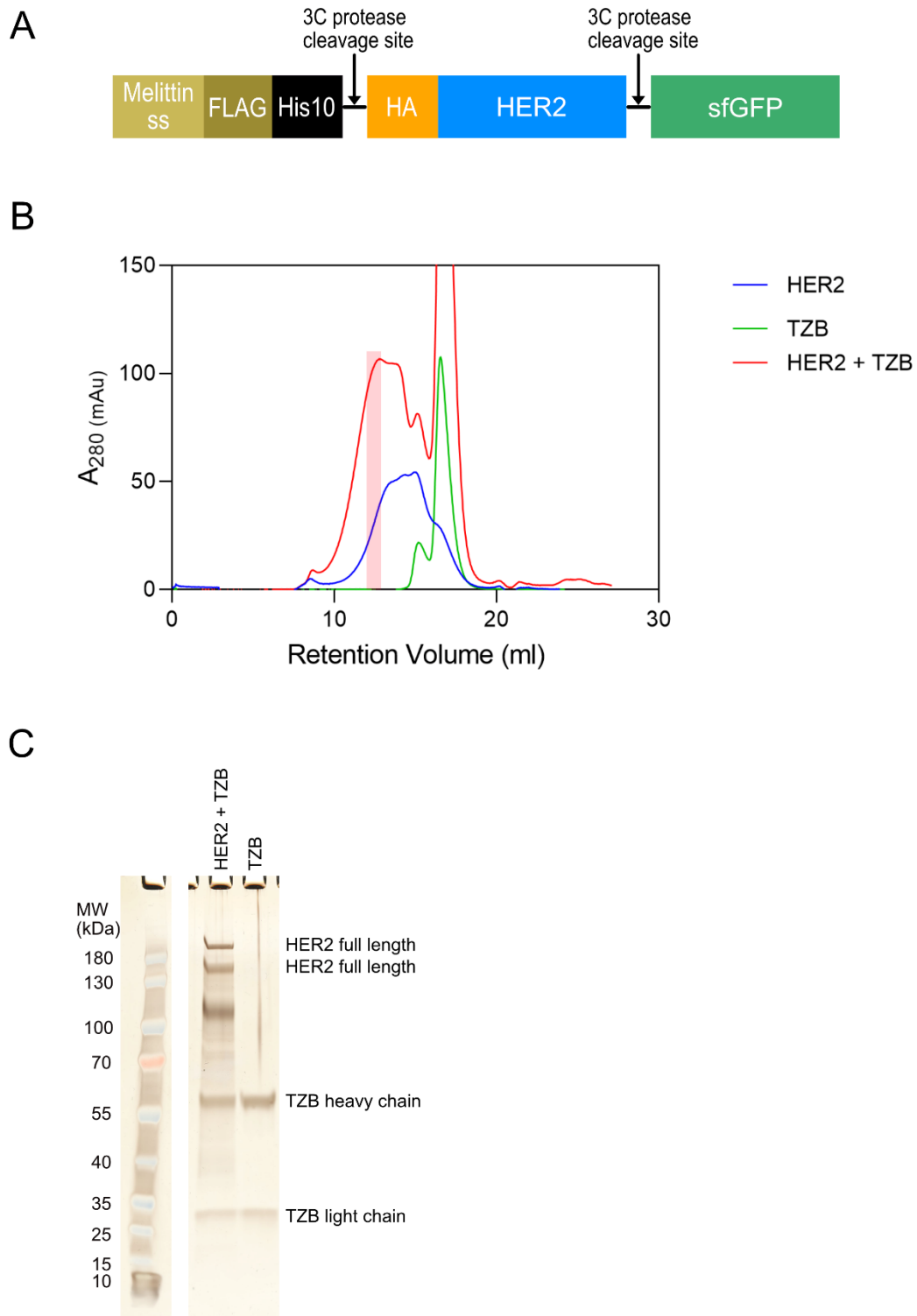


Figure S1.

HER2 construct: SEC and LDS-PAGE. (A) Design of the expressed and purified HER2 construct. (B) Preparative SEC profile of the purified HER2-TZB complex with the collected fraction indicated by the red bar. (C) Silver-stained LDS-PAGE gel of the HER2-TZB complex collected after SEC.

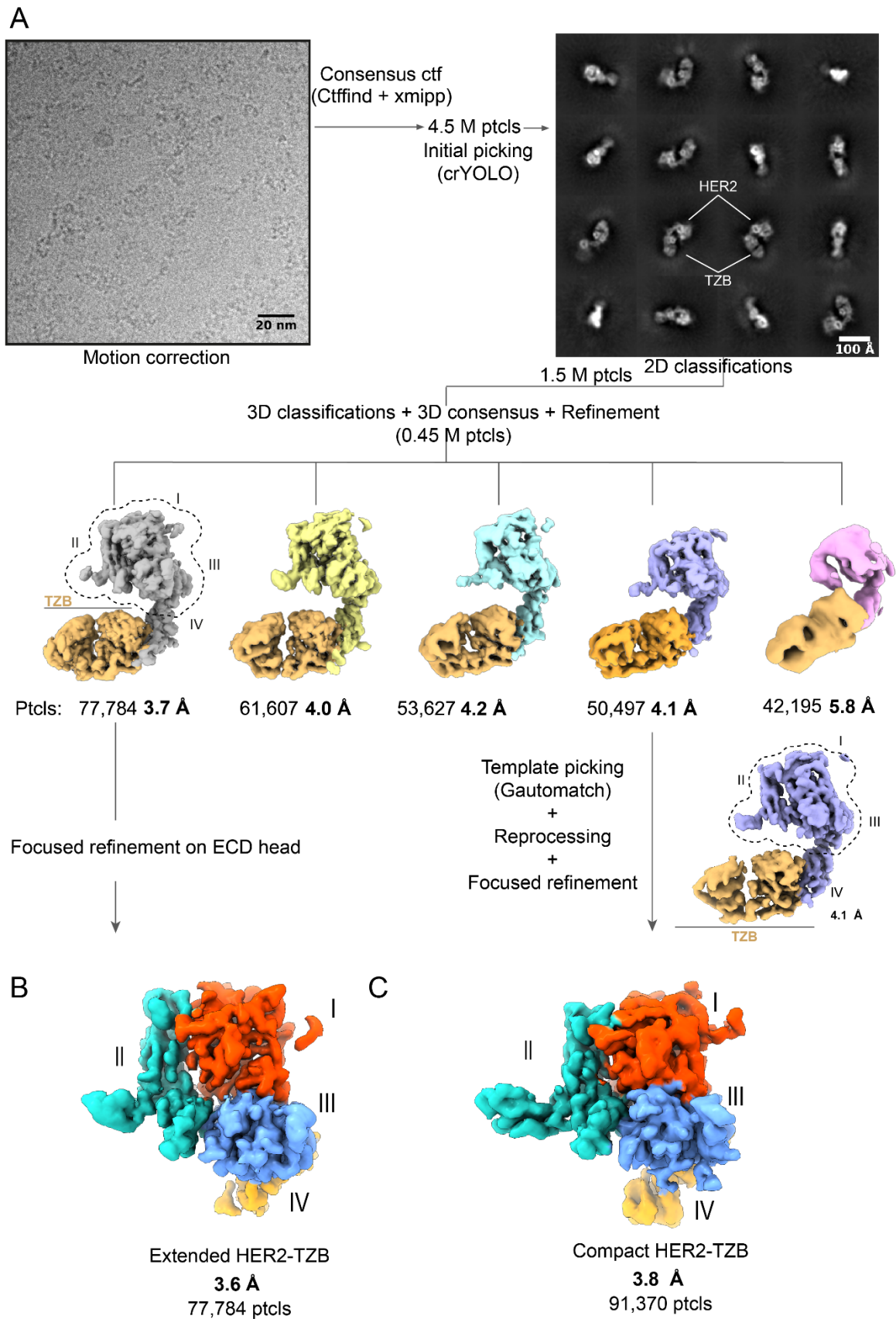


Figure S2.

Comprehensive workflow for cryo-EM data processing of HER2-TZB dataset showing the extended and compact HER2 conformations in complex with TZB. (A) (Left panel)

Representative cryo-EM micrograph of the HER2-TZB preparation. Scale bar: 20 nm. (Right panel) Gallery of 2D averages showing distinct secondary structure features from different views of the complex. Densities of HER2 ECD and TZB Fab are marked for a few of them. Scale bar: 100 Å. (Bottom panel) Output 3D classes after several rounds of 3D classifications and 3D consensus (see Methods). TZB has been colored in light brown to facilitate its identification in the density maps. The number of particles and resolution in Å (bold) are indicated below each class. Dashed outline around the ECD head in the extended (gray) and compact (purple) classes indicates the boundaries of the mask used for focused refinement in downstream steps. **(B)** Sharpened volume showing the extended conformation of HER2-TZB after focused refinement on the ECD head. **(C)** Sharpened volume of the compact HER2-TZB after increasing the number of particles of this conformation, followed by focused refinement on the ECD head. Subdomains are colored as in Fig. 1.

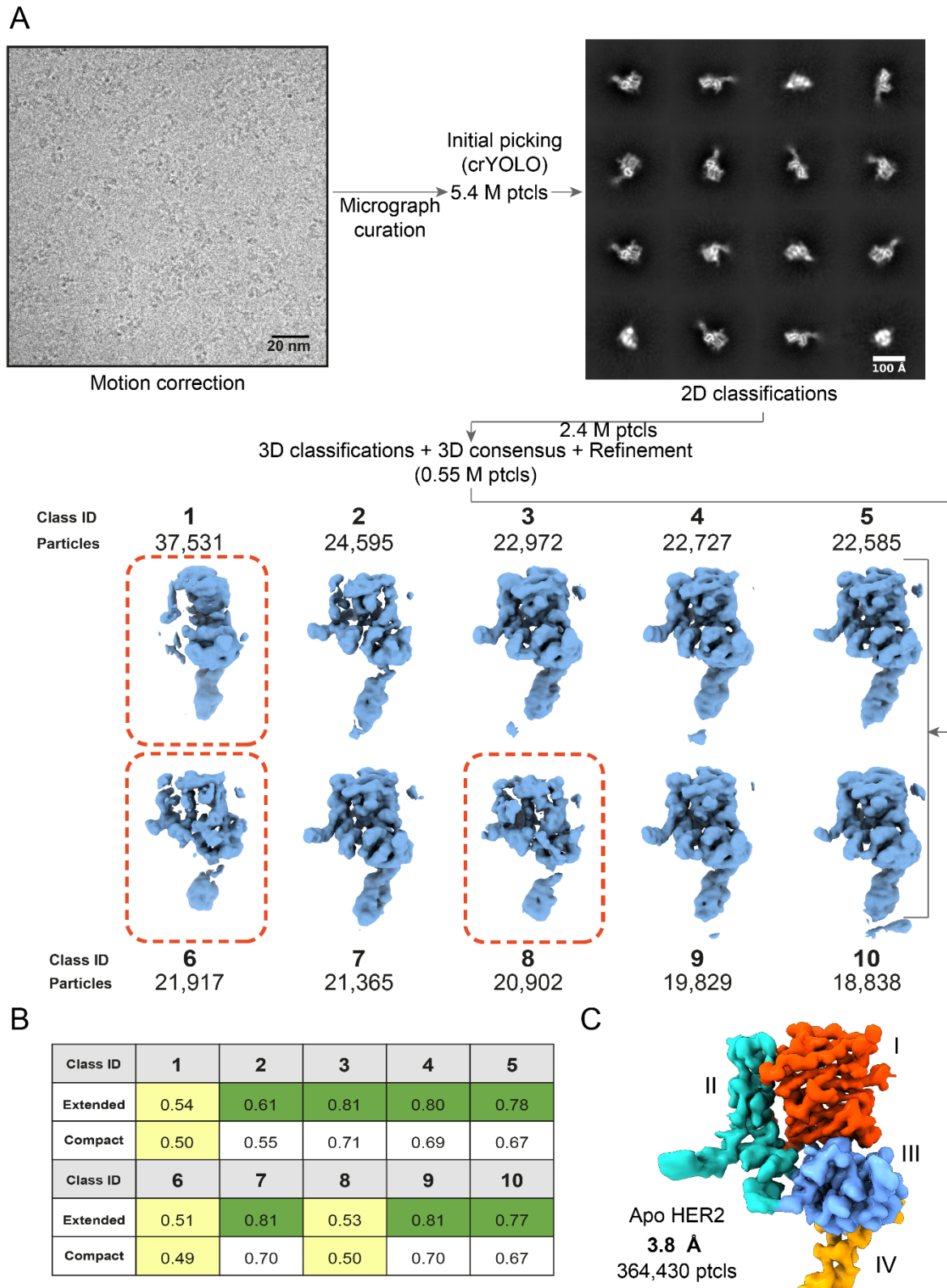


Figure S3.

Workflow for cryo-EM data processing of HER2 in the absence of trastuzumab (Apo dataset). (A) (Left panel) Representative cryo-EM micrograph of the HER2 preparation. Scale bar: 20 nm. (Right panel) Representative 2D averages showing distinct secondary structure

features from different views of the complex. Scale bar: 100 Å. (Bottom panel) The 10 top 3D classes obtained after several rounds of 3D classifications and 3D consensus are shown (see Methods). Doubtful classes potentially compatible (although at worse resolution) with a compact conformation of the receptor without TZB are displayed inside dashed squares. **(B)** Table with correlation coefficients between maps of the extended and compact ECDs from Fig. 1B, C with each of the output classes. For each pair, the highest value is highlighted in green, and always correspond to the extended conformation. Yellow cells indicate similar correlation values (difference < 0.05). **(C)** Sharpened volume after focused refinement on the ECD head, after SPA of the Apo dataset. Subdomains are colored as in Fig. 1.

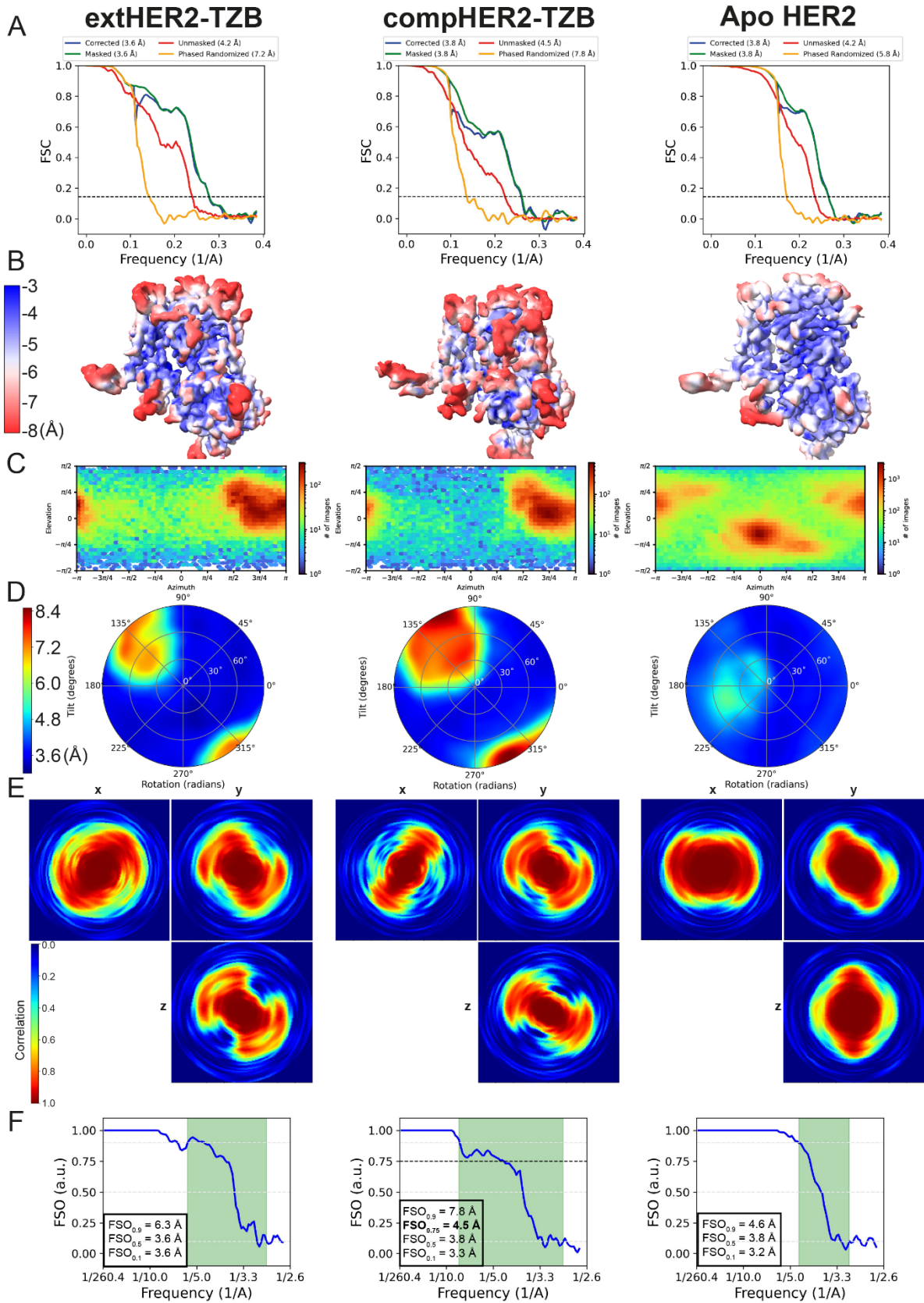


Figure S4.

Validation metrics for the extHER2-TZB, compHER2-TZB and Apo HER2 ECD head reconstructions. Panels in the same column correspond to the same reconstructed map. From

left to right: extHER2-TZB, compHER2-TZB (both from the TZB dataset) and the reconstruction from the Apo dataset. (A) Gold-standard Fourier Shell Correlation plots indicate the nominal resolution of each reconstruction. The horizontal dashed line highlights the correlation threshold at 0.143. (B) Local resolution maps. Sharpened maps were colored according to local resolution values calculated over half maps. (C) Particle distribution plots showing angular assignment after local refinement masking the ECD head. Note that extHER2-TZB and compHER2-TZB display similar distribution plots, as both reconstructions derive from the same dataset, distinct from that of the Apo reconstruction. (D) Directional resolution plots. Polar coordinates color plots display the resolution measured (in Å) for each direction. The Apo reconstruction shows a more uniform distribution, while for TZB-bound reconstructions the resolution ranges from 3 to 8 Å in certain directions. (E) 3D-Fourier Shell Correlation. Orthogonal slices in x, y and z axis of the 3D-FSC volume shows how the correlation between half maps decreases depending on the direction evaluated. Slices are colored according to the correlation value. (F) Fourier Shell Occupancy (FSO). FSO plots measure the fraction (occupancy) of all directions examined where the FSC is above an established threshold at a given resolution. At low resolution shells, FSO = 1, which means that the directional FSCs in all directions are above the threshold, so the map is fully isotropic at that spatial frequency. The green band is the anisotropy transition zone, where the fraction of directional FSCs above the threshold starts to fall, namely, the map gradually becomes anisotropic as the resolution increases. The start and end of this zone is set at resolutions where FSO = 0.9 and 0.1, respectively (inset and grey dashed lines). The resolution at FSO = 0.5 matches that reported by the FSC. Black dashed line in compHER2-TZB at FSO = 0.75 marks the maximum resolution considered for map depiction and modelling.

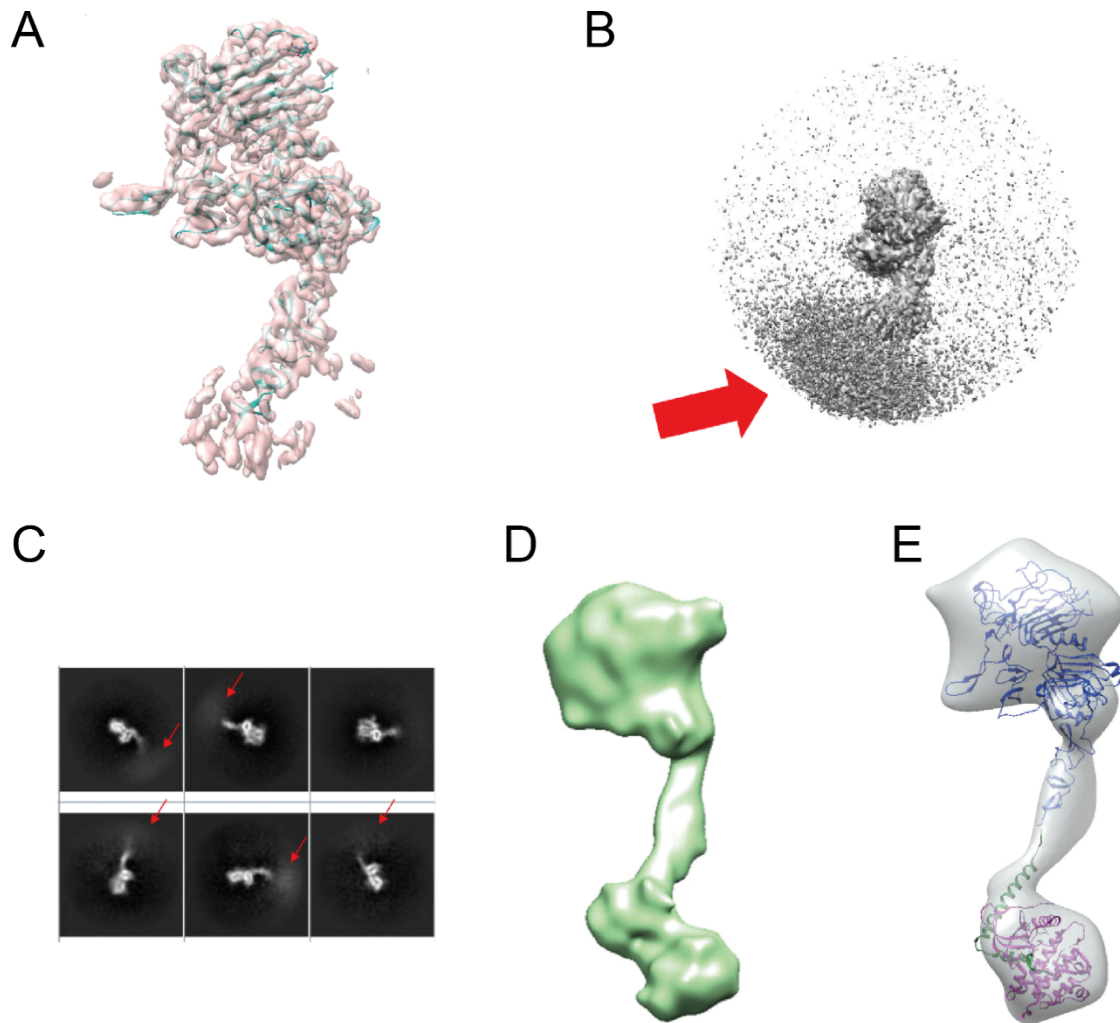


Figure S5.

Cryo-EM density maps of near full-length HER2 reconstituted in nanodiscs in the absence of TZB. (A) High-resolution cryo-EM map of the ECD of the near-full length HER2 reconstituted in a Saposin A-based nanodisc. In teal, the fitted HER2 ECD crystal structure (1N8Z). (B) Same reconstruction at lower contour level. The red arrow points to the unresolved density presumed to correspond to the HER2 transmembrane and kinase domains. (C) Representative 2D averages of the near-full length HER2 sample reconstituted in Saposin A-based nanodiscs. Red arrows point to the blurry density presumed to correspond to the HER2 transmembrane and kinase domains. (D) Low-resolution cryo-EM map of near-full length HER2 reconstituted in a Saposin A-based nanodisc. (E) Low-resolution cryo-EM map of near-full length HER2 reconstituted in a MSP-based nanodisc with manually fitted atomic models. Blue, HER2 ECD crystal structure (1N8Z). Green, HER2 transmembrane domain NMR structure (2N2A). Violet, HER2 kinase domain crystal structure (3PP0).

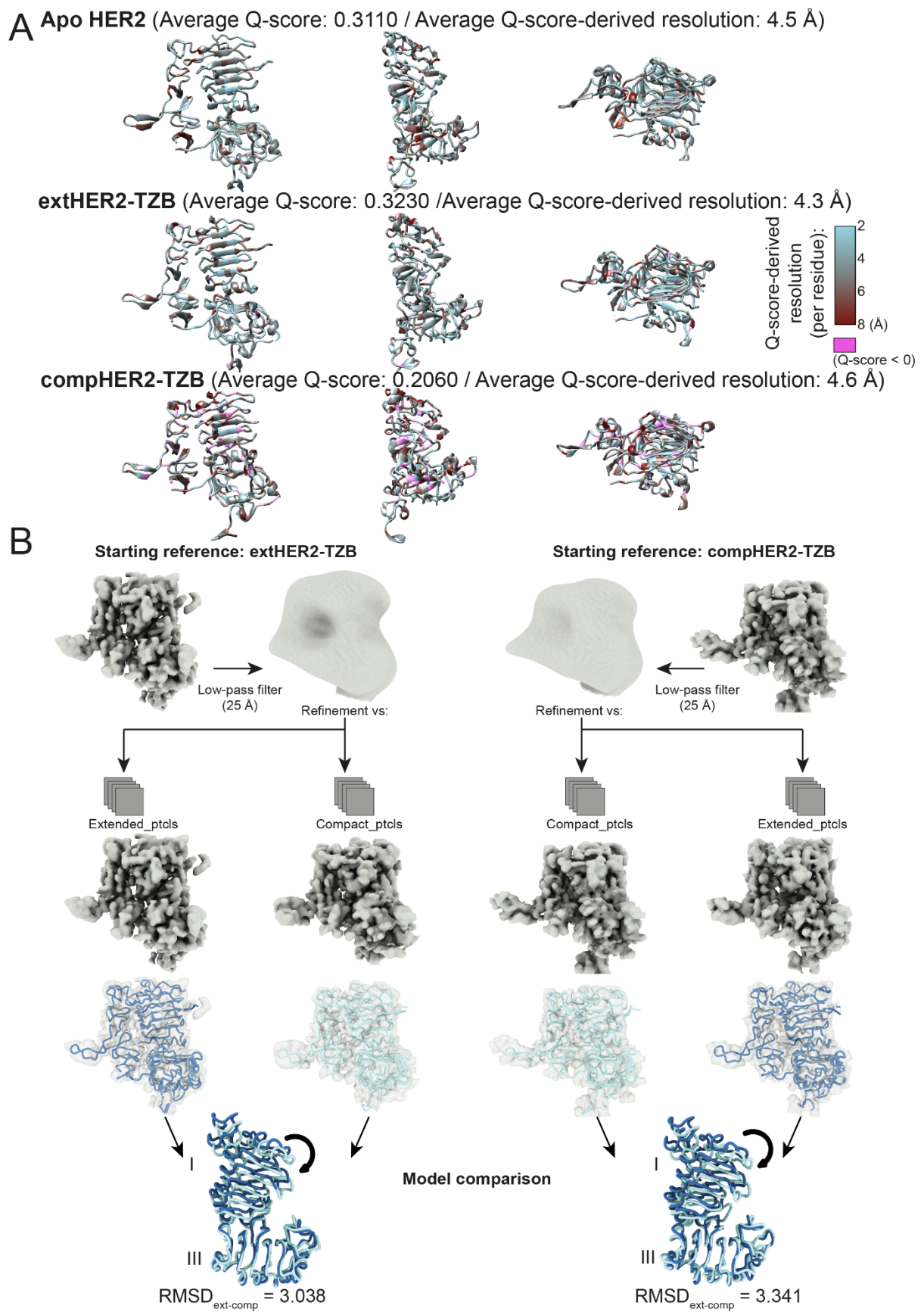


Figure S6.
Additional validations for the extHER2-TZB, compHER2-TZB and Apo HER2 ECD head reconstructions and models. (A) Average Q-score and average map resolution based on

average Q-score. Ribbon depictions of models in front, side and top views, respectively. Each residue is colored based on its resolution value derived from the per-residue Q-score (see Methods for more details), reflecting the resolution at which a given region of the reconstruction should be interpreted. Residues with negative Q-score values, which cannot be converted into a meaningful resolution value, are colored in pink. **(B)** Model bias validation for the TZB dataset, affected by certain preferred orientations. The starting reference (*i.e.* a compHER2-TZB or an extHER2-TZB map) was low-pass filtered to 25 Å and refined against either the particle stack of the same or the opposite conformation. When refined against particles of the same conformation as the starting volume, the starting volume was reproduced. When refined against the opposite particle stack, the conformation of the resulting map matches that of the particle stack. Next, the same model of HER2 ECD (from PDB 5MY6) was refined against each of the four maps. Models coming from maps that shared the same starting reference were aligned on subdomain III to calculate the RMSD, as in Fig. 3, to compare between each extended and compact pairs. Values for each pair were 3.038 (starting map: extended) and 3.341 (starting map: compact), similar to the value computed in Fig. 3B (3.124).

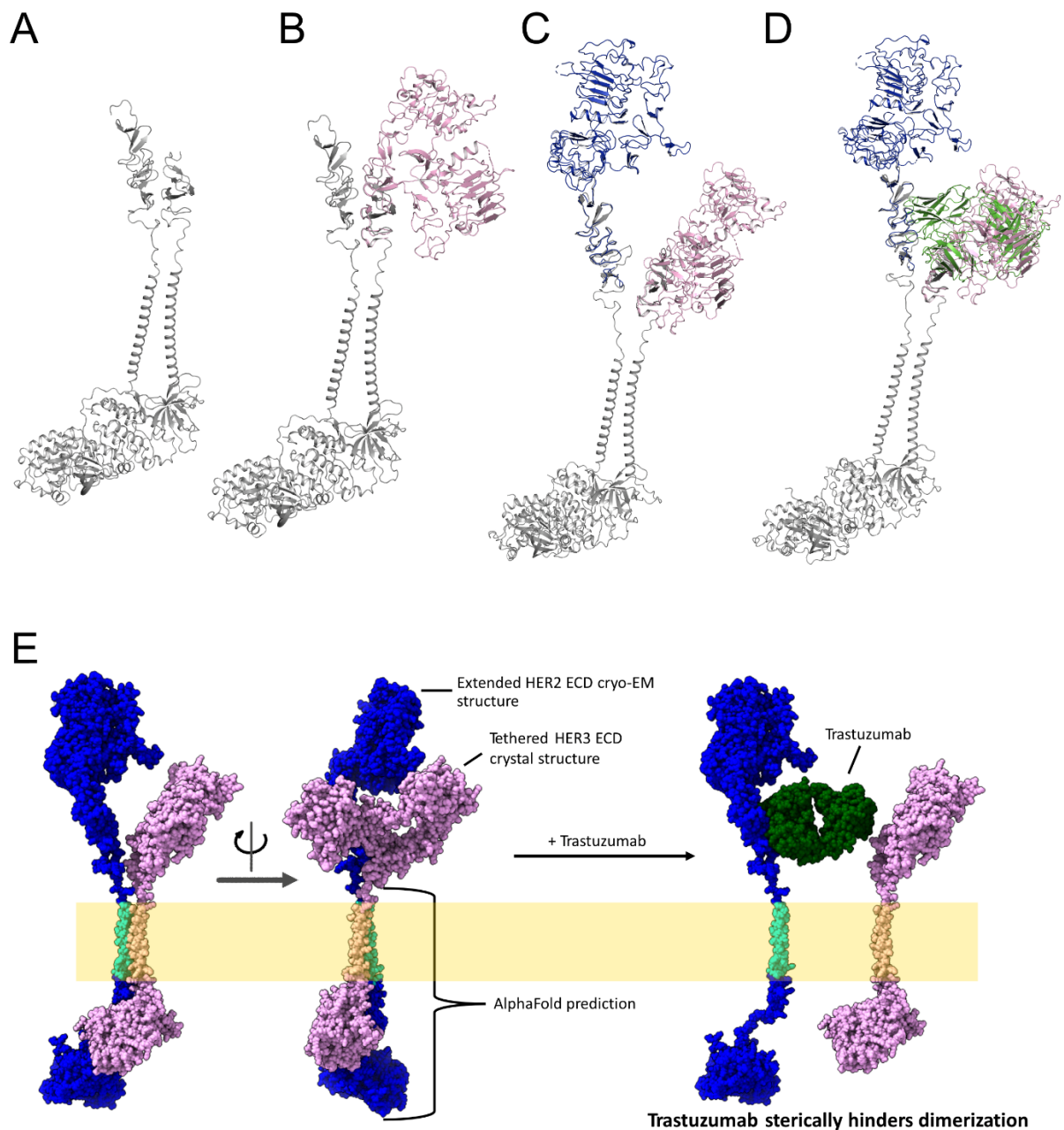


Figure S7.

Model of the TZB-induced inhibition of a HER2-HER3 ligand-independent heterodimer for the tethered HER3 conformation and the extended HER2 conformation. This model is merely meant as an indication about the likelihood of steric clashes and should therefore not be interpreted beyond this. (A) AlphaFold Multimer model of the HER2-HER3 heterodimer, with HER3 and HER2 in tethered and extended conformations, respectively. The model was built using HER2 residues 526-1029 and HER3 residues 569-979. The C-terminal tails and most of the ECD of both receptors were excluded from the input used for the model. (B) Superposition of the tethered HER3 ECD (PDB 4LEO, in pink) via subdomain IV onto the predicted structure, resulting in an RMSD of 0.770 Å. (C) Superposition of the extended HER2 ECD (in blue) without TZB via subdomain IV onto the predicted structure, resulting in an RMSD of 1.212 Å.

(D) Superposition of the extended ECD HER2-TZB complex (TZB in green) via subdomain IV onto the predicted structure, resulting in an RMSD of 1.212 Å. (E) Representation of the model on a schematic membrane surface. As in (C), no steric clashes are observed between HER3 and HER2 in the absence of TZB. On the other hand, steric clashes occur between HER2-bound TZB and the tethered HER3 ECD structure.

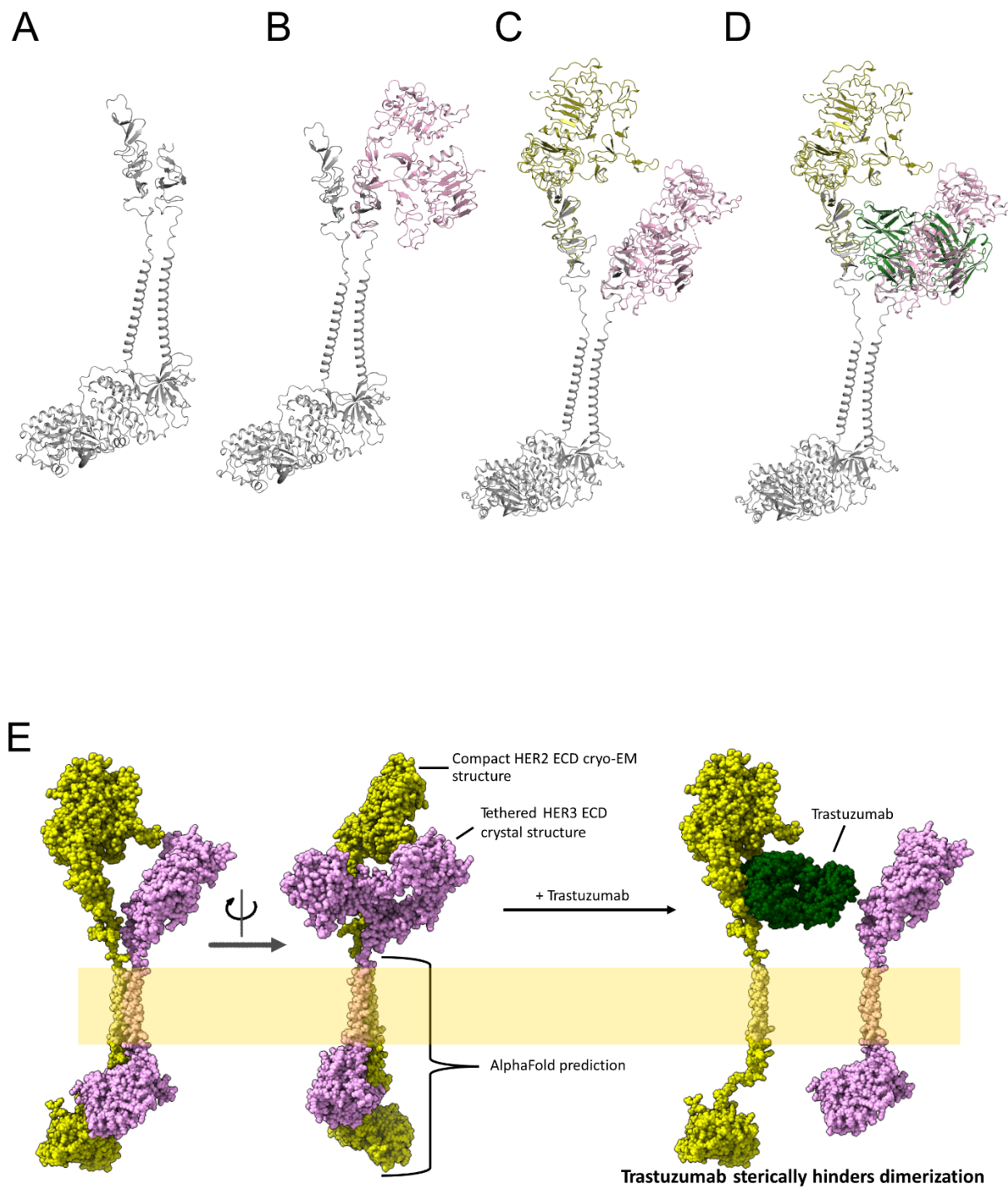


Figure S8.

Model of the TZB-induced inhibition of a HER2-HER3 ligand-independent heterodimer for the tethered HER3 conformation and the compact HER2 conformation. This model is merely meant as an indication about the likelihood of steric clashes and should therefore not be interpreted beyond this. (A) AlphaFold Multimer model of the HER2-HER3 heterodimer, with HER3 and HER2 in tethered and compact conformations, respectively. The model was built using HER2 residues 526-1029 and HER3 residues 569-979. The C-terminal tails and most of the ECD of both receptors were excluded from the input used for the model prediction. (B) Superposition of the tethered HER3 ECD (PDB 4LEO, in pink) via subdomain IV onto the predicted structure, resulting in an RMSD of 0.770 Å. (C) Superposition of the compact HER2

ECD (in olive green) without TZB via subdomain IV onto the predicted structure, resulting in an RMSD of 2.141 Å. **(D)** Superposition of the compact ECD HER2-TZB complex (TZB in green) via subdomain IV onto the predicted structure, resulting in an RMSD of 2.141 Å. **(E)** Representation of the model on a schematic membrane surface. As in (C), no steric clashes are observed between HER3 and HER2 in the absence of TZB. On the other hand, steric clashes occur between HER2-bound TZB and the tethered HER3 ECD structure.

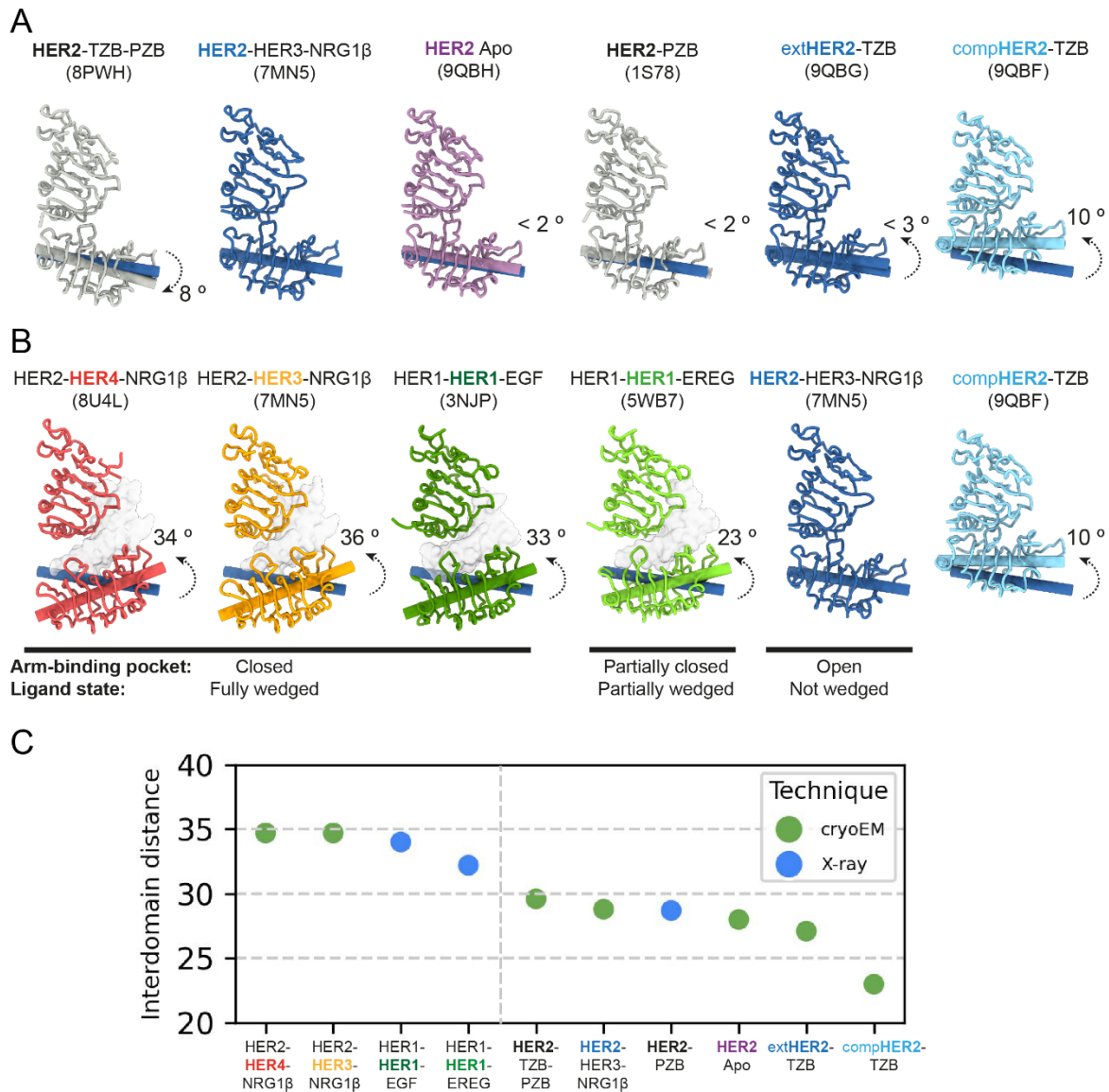


Figure S9.

Structural comparison of extended and compact models of this study with other structures of the EGFR family members. All HER structures were aligned on subdomain I, taking the HER2 model from the HER2-HER3-NRG1 β (PDB: 7MN5) as reference. Following a similar convention as in (30), the relative rotation between subdomains III in different models was calculated by measuring the angle between axes fitted along the longitudinal direction of each subdomain III. Such axis are also displayed for better visualization of the conformational change. Subdomain II and binding partners were omitted for clarity. Ligands are represented as semitransparent surfaces. For each structure, the model being shown is colored to match the color in the name above. (A) Relative rotation of subdomain III in several HER2 structures, including those from the present work. (B) Several degrees of opening of the dimerization arm-binding pocket in HER structures as a function of the ligand wedging state proposed in (30). Structures are grouped according to the ligand state. From left to right: Fully wedged (HER4, HER3 and HER1 from a symmetrical homodimer), partially wedged (HER1 from an asymmetrical homodimer) and not wedged (HER2 from heterodimer). The rightmost panel features compHER2-TZB. (C) Interdomain distance in Å between centroids of subdomains I

and III measured on the HER structures shown in (A) and (B). Colors indicate the experimental technique to obtain the structures. Vertical dashed line was added to separate measurements on HER2 from other EGFRs.

Movie S1.

Morphing between extHER2-TZB and compHER2-TZB models. Each subdomain is colored as in Fig. 1.

REFERENCES AND NOTES

1. Y. Yarden, M. X. Sliwkowski, Untangling the ErbB signalling network. *Nat. Rev. Mol. Cell Biol.* **2**, 127–137 (2001).
2. M. A. Olayioye, R. M. Neve, H. A. Lane, N. E. Hynes, The ErbB signaling network: Receptor heterodimerization in development and cancer. *EMBO J.* **19**, 3159–3167 (2000).
3. A. Arkhipov, Y. Shan, E. T. Kim, R. O. Dror, D. E. Shaw, Her2 activation mechanism reflects evolutionary preservation of asymmetric ectodomain dimers in the human EGFR family. *eLife* **2**, e00708 (2013).
4. C. Jost, J. C. Stüber, A. Honegger, Y. Wu, A. Batyuk, A. Plückthun, Rigidity of the extracellular part of HER2: Evidence from engineering subdomain interfaces and shared-helix DARPIn-DARPIn fusions. *Protein Sci.* **26**, 1796–1806 (2017).
5. H. S. Cho, K. Mason, K. X. Ramyar, A. M. Stanley, S. B. Gabelli, D. W. Denney Jr., D. J. Leahy, Structure of the extracellular region of HER2 alone and in complex with the Herceptin Fab. *Nature* **421**, 756–760 (2003).
6. D. Graus-Porta, R. R. Beerli, J. M. Daly, N. E. Hynes, ErbB-2, the preferred heterodimerization partner of all ErbB receptors, is a mediator of lateral signaling. *EMBO J.* **16**, 1647–1655 (1997).
7. Y. Yarden, A. Ullrich, Growth factor receptor tyrosine kinases. *Annu. Rev. Biochem.* **57**, 443–478 (1988).
8. G. Carpenter, S. Cohen, Epidermal growth factor. *J. Biol. Chem.* **265**, 7709–7712 (1990).
9. J. Baselga, S. M. Swain, Novel anticancer targets: Revisiting ERBB2 and discovering ERBB3. *Nat. Rev. Cancer* **9**, 463–475 (2009).
10. R. Roskoski Jr., The ErbB/HER family of protein-tyrosine kinases and cancer. *Pharmacol. Res.* **79**, 34–74 (2014).

11. J. Baselga, Why the epidermal growth factor receptor? The rationale for cancer therapy. *Oncologist* **7**, 2–8 (2002).
12. M. A. Lemmon, J. Schlessinger, Cell signaling by receptor tyrosine kinases. *Cell* **141**, 1117–1134 (2010).
13. P. Wu, T. E. Nielsen, M. H. Clausen, FDA-approved small-molecule kinase inhibitors. *Trends Pharmacol. Sci.* **36**, 422–439 (2015).
14. P. Wu, T. E. Nielsen, M. H. Clausen, Small-molecule kinase inhibitors: An analysis of FDA-approved drugs. *Drug Discov. Today* **21**, 5–10 (2016).
15. W. Cheng, Y. Hu, R. Sheng, Development of EGFR family small molecule inhibitors for anticancer intervention: An overview of approved drugs and clinical candidates. *Curr. Med. Chem.* **21**, 4374–4404 (2014).
16. N. E. Hynes, H. A. Lane, ERBB receptors and cancer: The complexity of targeted inhibitors. *Nat. Rev. Cancer* **5**, 341–354 (2005).
17. K. L. Blackwell, H. J. Burstein, A. M. Storniolo, H. S. Rugo, G. Sledge, G. Aktan, C. Ellis, A. Florance, S. Vukelja, J. Bischoff, J. Baselga, J. O’Shaughnessy, Overall survival benefit with lapatinib in combination with trastuzumab for patients with human Epidermal Growth Factor Receptor 2-positive metastatic breast cancer: Final results from the EGF104900 study. *J. Clin. Oncol.* **30**, 2585–2592 (2012).
18. C. E. Geyer, J. Forster, D. Lindquist, S. Chan, C. G. Romieu, T. Pienkowski, A. Jagiello-Gruszfeld, J. Crown, A. Chan, B. Kaufman, D. Skarlos, M. Campone, N. Davidson, M. Berger, C. Oliva, S. D. Rubin, S. Stein, D. Cameron, Lapatinib plus capecitabine for HER2-positive advanced breast cancer. *N. Engl. J. Med.* **355**, 2733–2743 (2006).
19. A. Di Leo, H. L. Gomez, Z. Aziz, Z. Zvirbule, J. Bines, M. C. Arbushites, S. F. Guerrero, M. Koehler, C. Oliva, S. H. Stein, L. S. Williams, J. Dering, R. S. Finn, M. F. Press, Phase III, double-blind, randomized study comparing lapatinib plus paclitaxel with placebo plus

- paclitaxel as first-line treatment for metastatic breast cancer. *J. Clin. Oncol.* **26**, 5544–5552 (2008).
20. S. T. Lee-Hoeflich, L. Crocker, E. Yao, T. Pham, X. Munroe, K. P. Hoeflich, M. X. Sliwkowski, H. M. Stern, A central role for HER3 in HER2-amplified breast cancer: Implications for targeted therapy. *Cancer Res.* **68**, 5878–5887 (2008).
21. S. M. Swain, D. Miles, S. B. Kim, Y. H. Im, S. A. Im, V. Semiglazov, E. Ciruelos, A. Schneeweiss, S. Loi, E. Monturus, E. Clark, A. Knott, E. Restuccia, M. C. Benyunes, J. Cortés, CLEOPARTRA study group, Pertuzumab, trastuzumab, and docetaxel for HER2-positive metastatic breast cancer (CLEOPATRA): End-of-study results from a double-blind, randomised, placebo-controlled, phase 3 study. *Lancet Oncol.* **21**, 519–530 (2020).
22. R. Nahta, M. C. Hung, F. J. Esteva, The HER-2-targeting antibodies trastuzumab and pertuzumab synergistically inhibit the survival of breast cancer cells. *Cancer Res.* **64**, 2343–2346 (2004).
23. J. Yu, T. Fang, C. Yun, X. Liu, X. Cai, Antibody-drug conjugates targeting the human epidermal growth factor receptor family in cancers. *Front. Mol. Biosci.* **9**, 847835 (2022).
24. M. Alimandi, A. Romano, M. C. Curia, R. Muraro, P. Fedi, S. A. Aaronson, P. P. Di Fiore, M. H. Kraus, Cooperative signaling of ErbB3 and ErbB2 in neoplastic transformation and human mammary carcinomas. *Oncogene* **10**, 1813–1821 (1995).
25. D. B. Vaught, J. C. Stanford, C. Young, D. J. Hicks, F. Wheeler, C. Rinehart, V. Sánchez, J. Koland, W. J. Muller, C. L. Arteaga, R. S. Cook, HER3 is required for HER2-induced preneoplastic changes to the breast epithelium and tumor formation. *Cancer Res.* **72**, 2672–2682 (2012).
26. T. Holbro, R. R. Beerli, F. Maurer, M. Koziczak, C. F. Barbas III, N. E. Hynes, The ErbB2/ErbB3 heterodimer functions as an oncogenic unit: ErbB2 requires ErbB3 to drive breast tumor cell proliferation. *Proc. Natl. Acad. Sci. U.S.A.* **100**, 8933–8938 (2003).

27. D. B. Agus, R. W. Akita, W. D. Fox, G. D. Lewis, B. Higgins, P. I. Pisacane, J. A. Lofgren, C. Tindell, D. P. Evans, K. Maiese, H. I. Scher, M. X. Sliwkowski, Targeting ligand-activated ErbB2 signaling inhibits breast and prostate tumor growth. *Cancer Cell* **2**, 127–137 (2002).
28. O. Metzger-Filho, E. P. Winer, I. Krop, Pertuzumab: Optimizing HER2 blockade. *Clin. Cancer Res.* **19**, 5552–5556 (2013).
29. R. Ghosh, A. Narasanna, S. E. Wang, S. Liu, A. Chakrabarty, J. M. Balko, A. M. González-Angulo, G. B. Mills, E. Penuel, J. Winslow, J. Sperinde, R. Dua, S. Pidaparathi, A. Mukherjee, K. Leitzel, W. J. Kostler, A. Lipton, M. Bates, C. L. Arteaga, Trastuzumab has preferential activity against breast cancers driven by HER2 homodimers. *Cancer Res.* **71**, 1871–1882 (2011).
30. D. Diwanji, R. Trenker, T. M. Thaker, F. Wang, D. A. Agard, K. A. Verba, N. Jura, Structures of the HER2-HER3-NRG1 β complex reveal a dynamic dimer interface. *Nature* **600**, 339–343 (2021).
31. Y. Hao, X. Yu, Y. Bai, H. J. McBride, X. Huang, Cryo-EM structure of HER2-trastuzumab-pertuzumab complex. *PLOS ONE* **14**, e0216095 (2019).
32. T. P. Garrett, N. M. McKern, M. Lou, T. C. Elleman, T. E. Adams, G. O. Lovrecz, M. Kofler, R. N. Jorissen, E. C. Nice, A. W. Burgess, C. W. Ward, The crystal structure of a truncated ErbB2 ectodomain reveals an active conformation, poised to interact with other ErbB receptors. *Mol. Cell* **11**, 495–505 (2003).
33. K. Aertgeerts, R. Skene, J. Yano, B. C. Sang, H. Zou, G. Snell, A. Jennings, K. Iwamoto, N. Habuka, A. Hirokawa, T. Ishikawa, T. Tanaka, H. Miki, Y. Ohta, S. Sogabe, Structural analysis of the mechanism of inhibition and allosteric activation of the kinase domain of HER2 protein. *J. Biol. Chem.* **286**, 18756–18765 (2011).
34. E. V. Bocharov, K. S. Mineev, P. E. Volynsky, Y. S. Ermolyuk, E. N. Tkach, A. G. Sobol, V. V. Chupin, M. P. Kirpichnikov, R. G. Efremov, A. S. Arseniev, Spatial structure of the dimeric transmembrane domain of the growth factor receptor ErbB2 presumably corresponding to the receptor active state. *J. Biol. Chem.* **283**, 6950–6956 (2008).

35. C. Jost, J. Schilling, R. Tamaskovic, M. Schwill, A. Honegger, A. Plückthun, Structural basis for eliciting a cytotoxic effect in HER2-overexpressing cancer cells via binding to the extracellular domain of HER2. *Structure* **21**, 1979–1991 (2013).
36. P. E. Bragin, K. S. Mineev, O. V. Bocharova, P. E. Volynsky, E. V. Bocharov, A. S. Arseniev, HER2 transmembrane domain dimerization coupled with self-association of membrane-embedded cytoplasmic juxtamembrane regions. *J. Mol. Biol.* **428**, 52–61 (2016).
37. J. F. Franco-Gonzalez, V. L. Cruz, J. Ramos, J. Martinez-Salazar, Conformational flexibility of the ErbB2 ectodomain and trastuzumab antibody complex as revealed by molecular dynamics and principal component analysis. *J. Mol. Model.* **19**, 1227–1236 (2013).
38. T. T. Junttila, R. W. Akita, K. Parsons, C. Fields, G. D. Lewis Phillips, L. S. Friedman, D. Sampath, M. X. Sliwkowski, Ligand-independent HER2/HER3/PI3K complex is disrupted by trastuzumab and is effectively inhibited by the PI3K inhibitor GDC-0941. *Cancer Cell* **15**, 429–440 (2009).
39. R. Ruedas, R. Vuillemot, T. Tubiana, J. M. Winter, L. Pieri, A. A. Arteni, C. Samson, S. Jonic, M. Mathieu, S. Bressanelli, Structure and conformational variability of the HER2-trastuzumab-pertuzumab complex. *J. Struct. Biol.* **216**, 108095 (2024).
40. H. Maadi, M. H. Soheilifar, W. S. Choi, A. Moshtaghian, Z. Wang, Trastuzumab mechanism of action; 20 years of research to unravel a dilemma. *Cancers (Basel)* **13**, 3540 (2021).
41. L. Z. Mi, M. J. Grey, N. Nishida, T. Walz, C. Lu, T. A. Springer, Functional and structural stability of the epidermal growth factor receptor in detergent micelles and phospholipid nanodiscs. *Biochemistry* **47**, 10314–10323 (2008).
42. L. Z. Mi, C. Lu, Z. Li, N. Nishida, T. Walz, T. A. Springer, Simultaneous visualization of the extracellular and cytoplasmic domains of the epidermal growth factor receptor. *Nat. Struct. Mol. Biol.* **18**, 984–989 (2011).
43. C. O. S. Sorzano, A. Jiménez-Moreno, D. Maluenda, E. Ramirez-Aportela, M. Martínez, A. Cuervo, R. Melero, J. J. Conesa, R. Sanchez-Garcia, D. Strelak, J. Filipovic, E. Fernandez-

- Gimenez, F. de Isidro-Gomez, D. Herreros, P. Conesa, L. Del Cano, Y. Fonseca, J. J. de la Morena, J. R. Macias, P. Losana, R. Marabini, J. M. Carazo, Image processing in cryo-electron microscopy of single particles: The power of combining methods. *Methods Mol. Biol.* **2305**, 257–289 (2021).
44. Y. Huang, J. Ognjenovic, D. Karandur, K. Miller, A. Merk, S. Subramaniam, J. Kuriyan, A molecular mechanism for the generation of ligand-dependent differential outputs by the epidermal growth factor receptor. *eLife* **10**, e73218 (2021).
45. R. Trenker, D. Diwanji, T. Bingham, K. A. Verba, N. Jura, Structural dynamics of the active HER4 and HER2/HER4 complexes is finely tuned by different growth factors and glycosylation. *eLife* **12**, RP92873 (2024).
46. J. L. Vilas, H. D. Tagare, New measures of anisotropy of cryo-EM maps. *Nat. Methods* **20**, 1021–1024 (2023).
47. J. Li, E. Choi, H. Yu, X. C. Bai, Structural basis of the activation of type 1 insulin-like growth factor receptor. *Nat. Commun.* **10**, 4567 (2019).
48. E. Uchikawa, E. Choi, G. Shang, H. Yu, X. C. Bai, Activation mechanism of the insulin receptor revealed by cryo-EM structure of the fully liganded receptor-ligand complex. *eLife* **8**, e48630 (2019).
49. X. Zhang, D. Yu, J. Sun, Y. Wu, J. Gong, X. Li, L. Liu, S. Liu, J. Liu, Y. Wu, D. Li, Y. Ma, X. Han, Y. Zhu, Z. Wu, Y. Wang, Q. Ouyang, T. Wang, Visualization of ligand-bound ectodomain assembly in the full-length human IGF-1 receptor by cryo-EM single-particle analysis. *Structure* **28**, 555–561.e4 (2020).
50. R. Tamaskovic, M. Schwill, G. Nagy-Davidescu, C. Jost, D. C. Schaefer, W. P. Verdurmen, J. V. Schaefer, A. Honegger, A. Plückthun, Intermolecular biparatopic trapping of ErbB2 prevents compensatory activation of PI3K/AKT via RAS-p110 crosstalk. *Nat. Commun.* **7**, 11672 (2016).

51. F. Kast, M. Schwill, J. C. Stüber, S. Pfundstein, G. Nagy-Davidescu, J. M. M. Rodríguez, F. Seehusen, C. P. Richter, A. Honegger, K. P. Hartmann, T. G. Weber, F. Kroener, P. Ernst, J. Piehler, A. Plückthun, Engineering an anti-HER2 biparatopic antibody with a multimodal mechanism of action. *Nat. Commun.* **12**, 3790 (2021).
52. J. C. Stüber, C. P. Richter, J. S. Bellón, M. Schwill, I. König, B. Schuler, J. Piehler, A. Plückthun, Apoptosis-inducing anti-HER2 agents operate through oligomerization-induced receptor immobilization. *Commun. Biol.* **4**, 762 (2021).
53. J. F. Vega, J. Ramos, V. L. Cruz, E. Vicente-Alique, E. Sanchez-Sanchez, A. Sanchez-Fernandez, Y. Wang, P. Hu, J. Cortes, J. Martinez-Salazar, Molecular and hydrodynamic properties of human epidermal growth factor receptor HER2 extracellular domain and its homodimer: Experiments and multi-scale simulations. *Biochim. Biophys. Acta Gen. Subj.* **1861**, 2406–2416 (2017).
54. G. Fuentes, M. Scaltriti, J. Baselga, C. S. Verma, Synergy between trastuzumab and pertuzumab for human epidermal growth factor 2 (Her2) from colocalization: An in silico based mechanism. *Breast Cancer Res.* **13**, R54 (2011).
55. E. Lobner, A. S. Humm, K. Goritzer, G. Mlynek, M. G. Puchinger, C. Hasenhindl, F. Rüker, M. W. Traxlmayr, K. Djinovic-Carugo, C. Obinger, Fcab-HER2 interaction: A menage a trois. Lessons from x-ray and solution studies. *Structure* **25**, 878–889.e5 (2017).
56. Z. Wang, L. Cheng, G. Guo, B. Cheng, S. Hu, H. Zhang, Z. Zhu, L. Niu, Structural insight into a matured humanized monoclonal antibody HuA21 against HER2-overexpressing cancer cells. *Acta Crystallogr. D Struct. Biol.* **75**, 554–563 (2019).
57. M. D'Huyvetter, J. De Vos, C. Xavier, M. Pruszynski, Y. G. J. Sterckx, S. Massa, G. Raes, V. Caveliers, M. R. Zalutsky, T. Lahoutte, N. Devoogdt, (131)I-labeled anti-HER2 camelid sdAb as a theranostic tool in cancer treatment. *Clin. Cancer Res.* **23**, 6616–6628 (2017).

58. J. Bostrom, S. F. Yu, D. Kan, B. A. Appleton, C. V. Lee, K. Billeci, W. Man, F. Peale, S. Ross, C. Wiesmann, G. Fuh, Variants of the antibody Herceptin that interact with HER2 and VEGF at the antigen binding site. *Science* **323**, 1610–1614 (2009).
59. C. Eigenbrot, M. Ultsch, A. Dubnovitsky, L. Abrahmsen, T. Hard, Structural basis for high-affinity HER2 receptor binding by an engineered protein. *Proc. Natl. Acad. Sci. U.S.A.* **107**, 15039–15044 (2010).
60. X. Bai, P. Sun, X. Wang, C. Long, S. Liao, S. Dang, S. Zhuang, Y. Du, X. Zhang, N. Li, K. He, Z. Zhang, Structure and dynamics of the EGFR/HER2 heterodimer. *Cell Discov.* **9**, 18 (2023).
61. D. Diwanji, R. Trenker, N. Jura, K. A. Verba, Efficient expression, purification, and visualization by cryo-EM of unliganded near full-length HER3. *Methods Enzymol.* **667**, 611–632 (2022).
62. A. P. Garner, C. U. Bialucha, E. R. Sprague, J. T. Garrett, Q. Sheng, S. Li, O. Sineshchekova, P. Saxena, C. R. Sutton, D. Chen, Y. Chen, H. Wang, J. Liang, R. Das, R. Mosher, J. Gu, A. Huang, N. Haubst, C. Zehetmeier, M. Haberl, W. Elis, C. Kunz, A. B. Heidt, K. Herlihy, J. Murtie, A. Schuller, C. L. Arteaga, W. R. Sellers, S. A. Ettenberg, An antibody that locks HER3 in the inactive conformation inhibits tumor growth driven by HER2 or neuregulin. *Cancer Res.* **73**, 6024–6035 (2013).
63. M. C. Franklin, K. D. Carey, F. F. Vajdos, D. J. Leahy, A. M. de Vos, M. X. Sliwkowski, Insights into ErbB signaling from the structure of the ErbB2-pertuzumab complex. *Cancer Cell* **5**, 317–328 (2004).
64. N. Gaborit, C. Larbouret, J. Vallaghe, F. Peyrusson, C. Bascoul-Mollevi, E. Crapez, D. Azria, T. Chardes, M. A. Poul, G. Mathis, H. Bazin, A. Pelegrin, Time-resolved fluorescence resonance energy transfer (TR-FRET) to analyze the disruption of EGFR/HER2 dimers: A new method to evaluate the efficiency of targeted therapy using monoclonal antibodies. *J. Biol. Chem.* **286**, 11337–11345 (2011).

65. S. Q. Zheng, E. Palovcak, J. P. Armache, K. A. Verba, Y. Cheng, D. A. Agard, MotionCor2: Anisotropic correction of beam-induced motion for improved cryo-electron microscopy. *Nat. Methods* **14**, 331–332 (2017).
66. J. M. de la Rosa-Trevin, A. Quintana, L. Del Cano, A. Zaldivar, I. Foche, J. Gutierrez, J. Gomez-Blanco, J. Burguet-Castell, J. Cuenca-Alba, V. Abrishami, J. Vargas, J. Oton, G. Sharov, J. L. Vilas, J. Navas, P. Conesa, M. Kazemi, R. Marabini, C. O. Sorzano, J. M. Carazo, Scipion: A software framework toward integration, reproducibility and validation in 3D electron microscopy. *J. Struct. Biol.* **195**, 93–99 (2016).
67. A. Rohou, N. Grigorieff, CTFFIND4: Fast and accurate defocus estimation from electron micrographs. *J. Struct. Biol.* **192**, 216–221 (2015).
68. T. Wagner, F. Merino, M. Stabrin, T. Moriya, C. Antoni, A. Apelbaum, P. Hagel, O. Sitsel, T. Raisch, D. Prumbaum, D. Quentin, D. Roderer, S. Tacke, B. Siebolds, E. Schubert, T. R. Shaikh, P. Lill, C. Gatsogiannis, S. Raunser, SPHIRE-crYOLO is a fast and accurate fully automated particle picker for cryo-EM. *Commun. Biol.* **2**, 218 (2019).
69. A. Punjani, J. L. Rubinstein, D. J. Fleet, M. A. Brubaker, cryoSPARC: Algorithms for rapid unsupervised cryo-EM structure determination. *Nat. Methods* **14**, 290–296 (2017).
70. A. Punjani, H. Zhang, D. J. Fleet, Non-uniform refinement: Adaptive regularization improves single-particle cryo-EM reconstruction. *Nat. Methods* **17**, 1214–1221 (2020).
71. K. Zhang, Gautomatch (2017); <https://github.com/scipion-em/scipion-em-gautomatch>.
72. R. Sanchez-Garcia, J. Gomez-Blanco, A. Cuervo, J. M. Carazo, C. O. S. Sorzano, J. Vargas, DeepEMhancer: A deep learning solution for cryo-EM volume post-processing. *Commun. Biol.* **4**, 874 (2021).
73. J. Zivanov, T. Nakane, B. O. Forsberg, D. Kimanius, W. J. Hagen, E. Lindahl, S. H. Scheres, New tools for automated high-resolution cryo-EM structure determination in RELION-3. *eLife* **7**, e42166 (2018).

74. J. L. Vilas, H. D. Tagare, J. Vargas, J. M. Carazo, C. O. S. Sorzano, Measuring local-directional resolution and local anisotropy in cryo-EM maps. *Nat. Commun.* **11**, 55 (2020).
75. E. C. Meng, T. D. Goddard, E. F. Pettersen, G. S. Couch, Z. J. Pearson, J. H. Morris, T. E. Ferrin, UCSF ChimeraX: Tools for structure building and analysis. *Protein Sci.* **32**, e4792 (2023).
76. J. K. Leman, B. D. Weitzner, S. M. Lewis, J. Adolf-Bryfogle, N. Alam, R. F. Alford, M. Aprahamian, D. Baker, K. A. Barlow, P. Barth, B. Basanta, B. J. Bender, K. Blacklock, J. Bonet, S. E. Boyken, P. Bradley, C. Bystroff, P. Conway, S. Cooper, B. E. Correia, B. Coventry, R. Das, R. M. De Jong, F. DiMaio, L. Dsilva, R. Dunbrack, A. S. Ford, B. Frenz, D. Y. Fu, C. Geniesse, L. Goldschmidt, R. Gowthaman, J. J. Gray, D. Gront, S. Guffy, S. Horowitz, P. S. Huang, T. Huber, T. M. Jacobs, J. R. Jeliazkov, D. K. Johnson, K. Kappel, J. Karanicolas, H. Khakzad, K. R. Khar, S. D. Khare, F. Khatib, A. Khramushin, I. C. King, R. Kleffner, B. Koepnick, T. Kortemme, G. Kuenze, B. Kuhlman, D. Kuroda, J. W. Labonte, J. K. Lai, G. Lapidoth, A. Leaver-Fay, S. Lindert, T. Linsky, N. London, J. H. Lubin, S. Lyskov, J. Maguire, L. Malmstrom, E. Marcos, O. Marcu, N. A. Marze, J. Meiler, R. Moretti, V. K. Mulligan, S. Nerli, C. Norn, S. O'Conchuir, N. Ollikainen, S. Ovchinnikov, M. S. Pacella, X. Pan, H. Park, R. E. Pavlovicz, M. Pethe, B. G. Pierce, K. B. Pilla, B. Raveh, P. D. Renfrew, S. S. R. Burman, A. Rubenstein, M. F. Sauer, A. Scheck, W. Schief, O. Schueler-Furman, Y. Sedan, A. M. Sevy, N. G. Sgourakis, L. Shi, J. B. Siegel, D. A. Silva, S. Smith, Y. Song, A. Stein, M. Szegedy, F. D. Teets, S. B. Thyme, R. Y. Wang, A. Watkins, L. Zimmerman, R. Bonneau, Macromolecular modeling and design in Rosetta: Recent methods and frameworks. *Nat. Methods* **17**, 665–680 (2020).
77. D. Liebschner, P. V. Afonine, M. L. Baker, G. Bunkoczi, V. B. Chen, T. I. Croll, B. Hintze, L. W. Hung, S. Jain, A. J. McCoy, N. W. Moriarty, R. D. Oeffner, B. K. Poon, M. G. Prisant, R. J. Read, J. S. Richardson, D. C. Richardson, M. D. Sammito, O. V. Sobolev, D. H. Stockwell, T. C. Terwilliger, A. G. Urzhumtsev, L. L. Videau, C. J. Williams, P. D. Adams, Macromolecular structure determination using x-rays, neutrons and electrons: Recent developments in Phenix. *Acta Crystallogr. D Struct. Biol.* **75**, 861–877 (2019).

78. P. Emsley, B. Lohkamp, W. G. Scott, K. Cowtan, Features and development of Coot. *Acta Crystallogr. D Biol. Crystallogr.* **66**, 486–501 (2010).
79. G. Pintilie, K. Zhang, Z. Su, S. Li, M. F. Schmid, W. Chiu, Measurement of atom resolvability in cryo-EM maps with Q-scores. *Nat. Methods* **17**, 328–334 (2020).
80. E. Fernandez-Gimenez, M. Martinez, R. Sanchez-Garcia, R. Marabini, E. Ramirez-Aportela, P. Conesa, J. M. Carazo, C. O. S. Sorzano, Cryo-EM density maps adjustment for subtraction, consensus and sharpening. *J. Struct. Biol.* **213**, 107780 (2021).
81. M. Schuster, M. Deluigi, M. Pantic, S. Vacca, C. Baumann, D. J. Scott, A. Plückthun, O. Zerbe, Optimizing the α_{1B} -adrenergic receptor for solution NMR studies. *Biochim. Biophys. Acta Biomembr.* **1862**, 183354 (2020).
82. A. Flayhan, H. D. T. Mertens, Y. Ural-Blimke, M. Martinez Molledo, D. I. Svergun, C. Low, Saposin lipid nanoparticles: A highly versatile and modular tool for membrane protein research. *Structure* **26**, 345–355.e5 (2018).
83. J. Jumper, R. Evans, A. Pritzel, T. Green, M. Figurnov, O. Ronneberger, K. Tunyasuvunakool, R. Bates, A. Zidek, A. Potapenko, A. Bridgland, C. Meyer, S. A. A. Kohl, A. J. Ballard, A. Cowie, B. Romera-Paredes, S. Nikolov, R. Jain, J. Adler, T. Back, S. Petersen, D. Reiman, E. Clancy, M. Zielinski, M. Steinegger, M. Pacholska, T. Berghammer, S. Bodenstein, D. Silver, O. Vinyals, A. W. Senior, K. Kavukcuoglu, P. Kohli, D. Hassabis, Highly accurate protein structure prediction with AlphaFold. *Nature* **596**, 583–589 (2021).
84. R. Evans, M. O'Neill, A. Pritzel, N. Antropova, A. Senior, T. Green, A. Židek, R. Bates, S. Blackwell, J. Yim, O. Ronneberger, S. Bodenstein, M. Zielinski, A. Bridgland, A. Potapenko, A. Cowie, K. Tunyasuvunakool, R. Jain, E. Clancy, P. Kohli, J. Jumper, D. Hassabis, Protein complex prediction with AlphaFold-Multimer. bioRxiv 463034 [Preprint] (2022). <https://doi.org/10.1101/2021.10.04.463034>.
85. P. Littlefield, L. Liu, V. Mysore, Y. Shan, D. E. Shaw, N. Jura, Structural analysis of the EGFR/HER3 heterodimer reveals the molecular basis for activating HER3 mutations. *Sci. Signal.* **7**, ra114 (2014).

86. K. S. Mineev, N. F. Khabibullina, E. N. Lyukmanova, D. A. Dolgikh, M. P. Kirpichnikov, A. S. Arseniev, Spatial structure and dimer–monomer equilibrium of the ErbB3 transmembrane domain in DPC micelles. *Biochim. Biophys. Acta* **1808**, 2081–2088 (2011).
87. K. S. Mineev, E. V. Bocharov, Y. E. Pustovalova, O. V. Bocharova, V. V. Chupin, A. S. Arseniev, Spatial structure of the transmembrane domain heterodimer of ErbB1 and ErbB2 receptor tyrosine kinases. *J. Mol. Biol.* **400**, 231–243 (2010).
88. E. F. Pettersen, T. D. Goddard, C. C. Huang, E. C. Meng, G. S. Couch, T. I. Croll, J. H. Morris, T. E. Ferrin, UCSF ChimeraX: Structure visualization for researchers, educators, and developers. *Protein Sci.* **30**, 70–82 (2021).